IOP Publishing Journal of Physics: Condensed Matter
J. Phys.: Condens. Matter **26** (2014) 284109 (9pp) doi:10.1088/0953-8984/26/28/284109

Dynamics of electrical double layer formation in room-temperature ionic liquids under constant-current charging conditions

Xikai Jiang[1], Jingsong Huang[2], Hui Zhao[3], Bobby G Sumpter[2] and Rui Qiao[1,4]

[1] Department of Mechanical Engineering, Clemson University, Clemson, SC 29634, USA
[2] Center for Nanophase Materials Sciences and Computer Science and Mathematics Division, Oak Ridge National Laboratory, Bethel Valley Road, Oak Ridge, TN 37831, USA
[3] Department of Mechanical Engineering, University of Nevada, Las Vegas, NV 89154, USA

E-mail: rqiao@clemson.edu

Received 26 November 2013, revised 9 January 2014
Accepted for publication 21 January 2014
Published 12 June 2014

Abstract

We report detailed simulation results on the formation dynamics of an electrical double layer (EDL) inside an electrochemical cell featuring room-temperature ionic liquids (RTILs) enclosed between two planar electrodes. Under relatively small charging currents, the evolution of cell potential from molecular dynamics (MD) simulations during charging can be suitably predicted by the Landau–Ginzburg-type continuum model proposed recently (Bazant *et al* 2011 *Phys. Rev. Lett.* **106** 046102). Under very large charging currents, the cell potential from MD simulations shows pronounced oscillation during the initial stage of charging, a feature not captured by the continuum model. Such oscillation originates from the sequential growth of the ionic space charge layers near the electrode surface. This allows the evolution of EDLs in RTILs with time, an atomistic process difficult to visualize experimentally, to be studied by analyzing the cell potential under constant-current charging conditions. While the continuum model cannot predict the potential oscillation under such far-from-equilibrium charging conditions, it can nevertheless qualitatively capture the growth of cell potential during the later stage of charging. Improving the continuum model by introducing frequency-dependent dielectric constant and density-dependent ion diffusion coefficients may help to further extend the applicability of the model. The evolution of ion density profiles is also compared between the MD and the continuum model, showing good agreement.

Keywords: ionic transport, electrical double layers, room-temperature ionic liquids, non-equilibrium transport, molecular dynamics.

(Some figures may appear in colour only in the online journal)

1. Introduction

Electrical double layers (EDLs) play a fundamental role in numerous applications including electrical energy conversion and storage such as batteries, supercapacitors and dye-sensitized solar cells. The structure and dynamics of EDLs depend strongly on the nature of the electrified surfaces and the response of surrounding electrolytes at the interface. EDLs in room-temperature ionic liquids (RTILs) have received increased attention in recent years, as RTILs are emerging as ideal electrolytes for many electrochemical systems. Specifically, RTILs are a new class of electrolyte that is composed exclusively of ions but remains in the liquid state at room temperature [1, 2]. Because of their wide electrochemical window, excellent thermal stability, low vapor pressure and other unique

[4] www.clemson.edu/~rqiao.

properties, [1, 2] using RTILs as working electrolytes can surpass many important limitations of current electrochemical devices. For example, using RTILs allows the working voltage of supercapacitors to be increased beyond that of organic electrolytes (i.e., >3 V) and thus can greatly increase the energy density of supercapacitors, since the amount of energy stored increases quadratically with applied voltage.

The structure and capacitance of EDLs in RTILs under equilibrium conditions have been extensively studied both using experimental techniques, [3–9] and theoretically by analytical modeling, [10–12] atomistic simulations, [13–20] and classical density functional theory calculations [21]. Thanks to these works, many interesting phenomena such as over-screening, lattice saturation, alternating layering of ions near electrode surface and the diverse shape of capacitance–voltage curves are now reasonably well understood. Compared to the structure and capacitance studies, the dynamics of EDLs, which often controls the performance of electrochemical devices such as dye-sensitized solar cells and supercapacitors, has received much less attention. The existing theoretical works in this area fall into two categories. The first category focuses on the equilibrium dynamics of ions inside EDLs [22–26]. For example, the self-diffusion of ions near a graphite surface with different charge densities has been carefully analyzed and it was found that the self-diffusion of ions is strongly heterogeneous. Under high surface charge densities, the lateral diffusion of ions in the first counter-ion layer is actually faster than that in bulk RTILs. The second category of work focuses on the non-equilibrium dynamics aspects, which is closely related to the formation and relaxation of EDLs. In one of the earliest non-equilibrium dynamics studies, [27] the dynamics of EDL formation in molten salts was explored by reversing the sign of the charges on the wall atoms and following the subsequent evolution of the potential across the cell with time. It was found that the charge relaxation near the wall is very rapid due to the small-scale translation of ions and the large driving force from strong local electric fields. In a related work [28], the polarization relaxation of RTILs confined between two oppositely electrified walls was studied by switching off the external electric field and then monitoring the decay of potential in the electrolyte with time. It was discovered that the EDL relaxation consists of a fast process with a time scale of <0.2 ps that accounts for 80% of the potential drop and a slower process with a characteristic time of ∼8 ps; it was also shown that ion diffusion, which occurs on a much longer time scale, is not involved in the EDL relaxation process. More recently, the relaxation of EDLs at an RTIL–graphite interface was studied using two different approaches [29]. In both approaches, the EDLs are equilibrated initially before the studies of dynamics. The difference is that at the beginning of the simulations, the charges on the electrode surface are removed instantly in the first approach, while the electrical potential on the two electrodes was switched to the same value in the second approach. The EDL relaxation probed by the first approach is found to be a fast process occurring on a time scale of picoseconds. In comparison, the EDL relaxation probed by the second approach is found to occur on a time scale of hundreds of picoseconds, largely due to the slow ion diffusion involved during the EDL reorganization.

Since RTILs are solvent-free electrolytes and the classical Poisson–Nernst–Planck (PNP) equations, which neglect steric effects and ion–ion correlations, cannot accurately describe the dynamics of EDLs in concentrated electrolytes, [10, 12, 30] the above non-equilibrium studies on the formation and relaxation of EDLs are all based on molecular dynamics (MD) simulations. However, because of the recent breakthrough in the development of continuum models for EDLs in RTILs, continuum simulations of EDL formation in RTILs have become possible. For example, modified PNP equations, which take into account steric effects, have been developed and used to study the ion dynamics in electrochemical cells [30]. Most recently, Bazant, Storey and Kornyshev developed a Landau–Ginzburg-type continuum model (hereafter called BSK model) that can reproduce many essential features of EDLs in RTILs [12, 31]. Using such a model, the step charging of a parallel electrochemical cell was recently simulated, [32] and the results indicated that the essential behavior of charging (i.e., formation of the EDLs) is closely controlled by a new length scale $\sqrt{\lambda_D l_c}$, where λ_D is the Debye length and l_c is the correlation length in RTILs, and a time scale $\lambda_D^{3/2} L/(D l_c^{1/2})$, where D is the ion diffusion coefficient and L is the width of the electrochemical cell. The time scale is consistent with that inferred from the classical resistor–capacitor (RC) circuit model.

All of the above studies have provided fundamental insights into the formation and relaxation of EDLs in RTILs, but many issues remain to be explored, some of which are critically relevant to the practical applications of EDLs. First, the majority of the prior studies focused on the macroscopic behavior of EDL formation/relaxation by examining the variation of the electrical potential drop across EDLs, but relatively few works provided detailed characterizations for the evolution of EDL structures. Second, most of the existing works dealt with the limiting case of EDL formation or relaxation, i.e., when a step change of the charged state is enforced on the electrode surface. Such a limiting case corresponds to an infinitely large electronic current in the external electric circuit, which is not practical. Finally, although the recently developed BSK model [12] can reproduce many EDL properties under equilibrium condition, it is not yet clear whether it can predict the dynamics of EDL formation with accuracy. With these issues in mind, herein we study the dynamics of EDL formation in an electrochemical cell featuring a pair of planar electrodes separated by RTILs under constant-current charging conditions, a scenario widely encountered in galvanostatic electrochemical experiments. In particular, we examine the temporal evolution of the potential and ion density distribution across the entire cell under different charging currents using MD simulations. The results are compared with the continuum simulation results obtained using the BSK model.

2. Simulation systems and methods

MD simulations. The MD model for the electrochemical cell consists of two parallel walls and the RTIL electrolyte enclosed in between (figure 1). The separation between the two walls is 30 nm, which is wide enough to ensure bulk-like RTIL

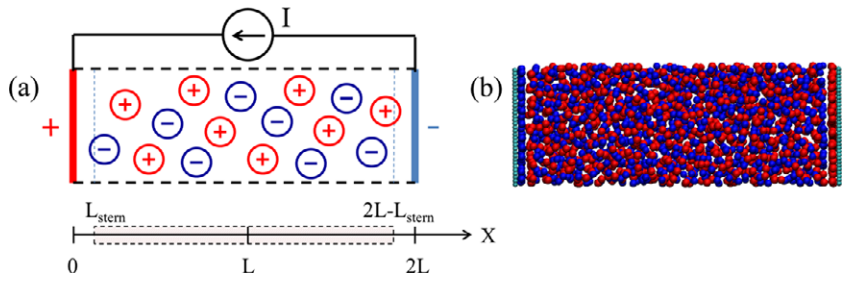

Figure 1. (a) Schematic of MD (top) and continuum models (bottom) used for studying the formation of EDLs at the interface of planar electrodes and RTILs. The electrical potential at $x = 0$ is taken as zero. The horizontal dashed lines in the top panel denote periodic boundaries of the MD system. (b) A snapshot of the MD system, where the blue and red spheres represent anions and cations, respectively.

behavior in the middle of the system. The force fields for the wall atoms and RTILs are the same as those adopted in [13]. Briefly, each wall is made of Lennard-Jones (LJ) spheres arranged in a square lattice with a lattice spacing of 0.33 nm. The ions are modeled as a generic RTIL without molecular details. Cations and anions of the RTIL electrolyte are symmetrical LJ spheres of 0.5 nm in radius with unit charge. The setup and the identical cation/anion radii lead to a symmetrical capacitor. The non-electrostatic interactions within the system are described by $u_{\mathrm{LJ}}(r) = \frac{C_{12}}{r^{12}}$, [13] where r is the distance between two atoms. At a temperature of $T = 450$ K, the LJ parameters are $C_{12} = 3.742$ kJ mol^{-1} nm^{-1} for ion–ion interactions and 9.931×10^{-3} kJ mol^{-1} nm^{-1} for ion–wall interactions [13]. A background dielectric constant of 2.0 is used in the calculations of electrostatic interactions to account for the electronic polarizability of ions not explicitly modeled in the force fields. We adopt this minimal model for RTILs because it has been shown to successfully capture the key features of EDLs revealed by simulations based on more sophisticated RTIL models [13]. The number of cation–anion pairs for the RTIL electrolyte is tuned so that the cation/anion concentration in the cell center is 0.5 M at zero wall charge conditions.

Simulations are performed in the NVT ($T = 450$ K) ensemble using the Gromacs package [33]. A time step of 5 fs is used. Further details of the MD technique, such as the calculations of electrostatic interactions and thermostating, can be found in our prior work on electrokinetic transport in RTILs [14]. Using the setup and force fields given above, we were able to accurately reproduce the capacitance–voltage (C–V) relation of EDLs under the equilibrium conditions reported in [13]. To simulate the formation of EDLs at the electrode/electrolyte interface under constant-current charging conditions, we first equilibrate the system with zero wall charge for 100 ns. At $t > 0$, we continuously add (remove) a small partial charge on each atom of the positive (negative) electrode wall until the absolute value of the surface charge density of both walls reaches 0.09 C m^{-2}. The rate at which the partial charge was added to (removed from) the positive (negative) wall atoms was varied to obtain five charging current densities: $I = 25$, 50, 100, 200 and 400 kA cm^{-2}. We note that these current densities are several orders of magnitude larger than that found in typical experimental systems [34, 35] because the spacing between the two charged walls is small and the diffusion coefficient of the model RTILs used here is large (see below). During simulations, the number densities of cations and anions across the cell are recorded every 1, 0.5, 0.25, 0.125 and 0.075 ps for the five different charging rates, respectively. To obtain reliable statistics, each charging case is repeated 100 times with independent initial configurations. The potential distribution across the entire cell is then calculated using the following equation derived from Poisson's equation [36]

$$\phi(x) = \frac{s}{\epsilon_0 \epsilon_r} x - \frac{1}{\epsilon_0 \epsilon_r} \int_0^x (x - y) \rho_{\mathrm{e}}(y) \mathrm{d}y \tag{1}$$

where ϕ is the electrical potential, s is the wall charge density, x is the distance from the geometrical plane of the left wall ($x = 0$), ϵ_0 is the vacuum permittivity, ϵ_r is the background dielectric constant used in the RTIL model and ρ_{e} is the ionic space charge density. As indicated in figure 1, the left wall is the positive electrode of the electrochemical cell, with its potential taken as zero.

Continuum simulations. Based on the BSK model developed in [12], the dynamics of EDL formation in the above system can be described by the following equations:

$$\frac{\partial C_\pm}{\partial t} = D_\pm \frac{\partial}{\partial x} \left(\frac{\partial C_\pm}{\partial x} \pm \frac{F}{RT} C_\pm \frac{\partial \phi}{\partial x} + \frac{\gamma C_\pm}{1 - \gamma (C_+ + C_-)} \frac{\partial (C_+ + C_-)}{\partial x} \right), \tag{2}$$

$$\epsilon_0 \epsilon_{\mathrm{bulk}} \left(l_{\mathrm{c}}^2 \frac{\partial^2}{\partial x^2} - 1 \right) \frac{\partial^2 \phi}{\partial x^2} = F (C_+ - C_-) \tag{3}$$

where $C_\pm$ are the cation/anion concentrations, R is the ideal gas constant, F is the Faraday constant, T is temperature, γ is the minimum volume available in space for ions, $D_\pm$ is the ion diffusion coefficient, ϵ_{bulk} is the permittivity of bulk RTILs and l_{c} is the electrostatic correlation length. An ion-free Stern layer with a thickness of L_{stern} and a dielectric constant of $\epsilon_{\mathrm{stern}}$ are also included near both walls (see figure 1). To facilitate the comparison of the predictions by the BSK model with those by the MD simulations, the BSK model is parameterized using the properties of the model RTILs described above. Part of such a parameterization has been performed in [12], and the results are as follows: $L_{\mathrm{stern}} = 0.5$ nm, $\gamma = 0.83$ nm^3, $l_{\mathrm{c}} = 1.33$ nm, $\epsilon_{\mathrm{bulk}} = \epsilon_{\mathrm{stern}} = 5$. To determine the diffusion

coefficient of the cation and anion, we perform independent simulations to compute the electrical mobility of ions by applying uniform electric fields to bulk RTILs. Next, the diffusion coefficient of ions is obtained by using the Einstein relation between diffusion coefficient and electrical mobility. This method is consistent with the fact that the Einstein relation is assumed in equation (2). Using this method, $D_+ = D_- = 1.68 \times 10^{-8}$ m^2 s^{-1} was obtained. Such a diffusion coefficient is three to four orders of magnitude larger than that of typical bulk RTILs due to the spherical geometry of the RTIL model and the high temperature adopted here. Because of this large ion diffusion coefficient, the formation and relaxation of EDLs is fast. As such, it enables nearly quasi-equilibrium formation of EDLs to be simulated at a charging rate much larger than that in practical systems (e.g., $I = 25$ kA cm^{-2}, cf figure 6(a)), which facilitates the comparison with EDL formation under non-equilibrium charging conditions.

Equation (2) is complemented by a zero-ion flux boundary condition for the ions at $x = 0$ and $2L$. For equation (3), the third derivative of the electrical potential is set to zero at $x = 0$ and $2L$; the first derivative of the electrical potential at $x = 0$ and $2L$ is treated as a time-dependent function which represents the steady increase of the wall charge density due to constant-current charging:

$$\left.\frac{\partial \phi}{\partial x}\right|_{x=0} = \frac{-It}{\epsilon_0 \epsilon_{\text{bulk}}}; \qquad \left.\frac{\partial \phi}{\partial x}\right|_{x=2L} = \frac{It}{\epsilon_0 \epsilon_{\text{bulk}}} \tag{4}$$

where I is the current density (kA m^{-2}). At $t = 0$, $C_+ = C_- = 0.5$ M and $\phi = 0$ V throughout the domain. These equations were solved using a commercial finite element package Comsol [37, 38]. Non-uniform elements are implemented in order to better resolve EDLs near walls while minimizing the computational cost. Mesh sizes are reduced several times to ensure the results are mesh-independent. As in the MD simulations, five different constant charging current densities are used to study the dynamics of EDL formation.

3. MD results and discussions

We first examine the dynamics of EDL formations in the RTIL electrolyte using the MD method described in section 2. Figure 2 shows the evolutions of the potential drop across the entire cell as a function of the wall charge density under constant-current charging at different rates. At the highest charging rate ($I = 400$ kA cm^{-2}), the potential drop increases sharply as the wall charge density increases and oscillates significantly until the wall charge density reaches ~0.02 C m^{-2}. Afterward, the potential drop increases rather linearly with the wall charge density, and the weak curvature of the voltage–charge curve is closely related to the fact that the differential capacitance of double layers in RTILs depends on the surface charge density of the electrodes. At lower charging rates, the oscillation of potential drop across the cell initiates at lower wall charge densities and the amplitude is reduced with respect to that of 400 kA cm^{-2}. For any given wall charge density, the potential drop across the cell increases with increasing charging current, which is expected because higher

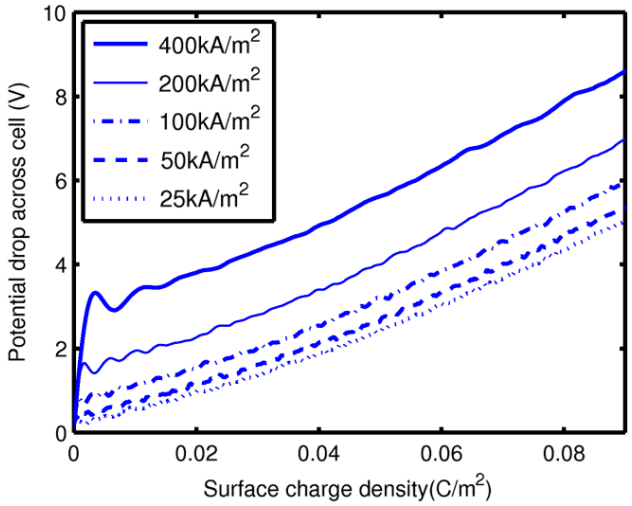

Figure 2. Evolution of the potential drop across the entire electrochemical cell (cf figure 1) as a function of the wall charge density during constant-current charging at different charging rates.

charging current leads to larger ionic current and IR drop across the RTILs (Ohmic loss), and thus larger voltage drop across the entire cell. These theoretical evolutions of potential drop bear a close resemblance to the charging branch of the galvanostatic charge/discharge profiles of supercapacitors utilizing RTILs as electrolytes, where the voltage plotted versus time shows linear slopes indicating capacitive behavior [34, 39]. We also note that the system has negative dynamic differential capacitance due to potential oscillations.

To understand the physical origins of the potential oscillation shown in figure 2, we examine the potential drop across half of the cell ϕ_{hc}, i.e., that from the left wall to the cell center. Note that ϕ_{hc} is 1/2 of the total potential drop across the entire cell due to the symmetries of the cell geometry and ion models used here. Using equation (1), the rate at which the half-cell potential drop ϕ_{hc} changes under a constant-current charging condition is given by

$$\frac{\partial \phi_{\text{hc}}}{\partial t} = \frac{\partial \phi_{\text{wc}}}{\partial t} + \frac{\partial \phi_{\text{ic}}}{\partial t} \tag{5a}$$

$$\frac{\partial \phi_{\text{wc}}}{\partial t} = \frac{IL}{\varepsilon_0 \epsilon_r} \tag{5b}$$

$$\frac{\partial \phi_{\text{ic}}}{\partial t} = -\frac{1}{\varepsilon_0 \epsilon_r} \frac{\partial \int_0^L (L-y)\rho_{\text{e}}(y)\mathrm{d}y}{\partial t}. \tag{5c}$$

In equation (5*a*), $\partial\phi_{\text{wc}}/\partial t$ and $\partial\phi_{\text{ic}}/\partial t$ represent the contributions from the accumulation of surface charge on the wall and from the formation of ionic space charge layers (i.e., EDLs) inside the RTILs, respectively. Note that $\partial\phi_{\text{wc}}/\partial t$ is a constant determined by the charging rate in the constant-current charging. Figure 3(a) shows the temporal evolution of ϕ_{hc}, while figure 3(b) shows the contributions to ϕ_{hc} from the two components of $\partial\phi_{\text{wc}}/\partial t$ and $\partial\phi_{\text{ic}}/\partial t$. Figure 3(b) indicates that the oscillation of the half-cell potential drop is driven by the dynamic formation of ionic space charge layers inside RTILs: ϕ_{hc} increases (decreases) whenever $|\partial\phi_{\text{ic}}/\partial t|$ is smaller (larger) than $\partial\phi_{\text{wc}}/\partial t$, and ϕ_{hc} reaches a peak (or valley) whenever $\partial\phi_{\text{ic}}/\partial t$ becomes equal to $\partial\phi_{\text{wc}}/\partial t$. More

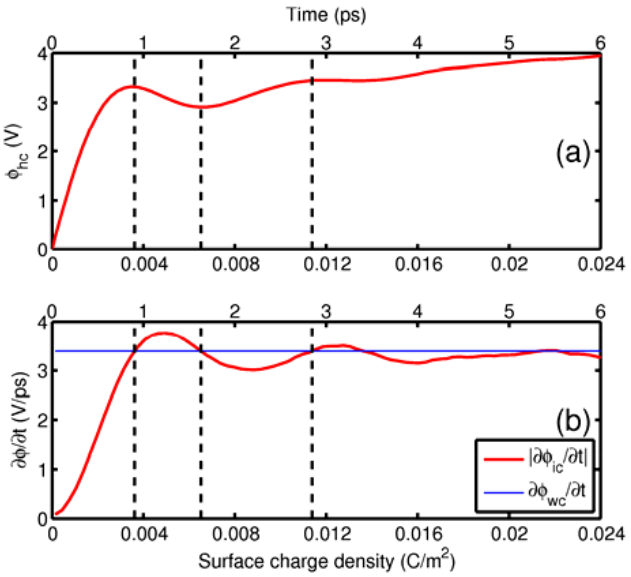

Figure 3. Evolution of the potential drop across a half-cell under the largest charging current studied ($I = 400$ kA cm^{-2}). (a) Temporal evolution of the half-cell potential drop (ϕ_{hc}); (b) contributions from the wall charge ($\partial\phi_{wc}/\partial t$, horizontal blue line) and the ionic space charge ($|\partial\phi_{ic}/\partial t|$, red curve) to the half-cell potential drop. Since $\partial\phi_{ic}/\partial t$ is always negative, its absolute value is shown here to facilitate comparison with $\partial\phi_{wc}/\partial t$. The vertical dashed lines denote the time when ϕ_{hc} reaches a peak (or valley) or equivalently when $\partial\phi_{wc}/\partial t$ is equal to $|\partial\phi_{ic}/\partial t|$.

specifically, for $t < 1.24$ ps, $\partial\phi_{ic}/\partial t$ increases rapidly and exceeds $\partial\phi_{wc}/\partial t$ at $t = 0.91$ ps and this leads to the first peak of ϕ_{hc}. Between $t = 1.24$ and 2.21 ps, $|\partial\phi_{ic}/\partial t|$ decreases and crosses over $\partial\phi_{wc}/\partial t$ at $t = 1.63$ ps, leading to the first valley of ϕ_{hc}. At later times, $|\partial\phi_{ic}/\partial t|$ still oscillates but with a reduced amplitude. As such, the oscillation of ϕ_{hc} becomes weaker with time and practically disappears at $t > 6$ ps.

The above results indicate that the formation of ionic space charge layers (or equivalently, EDLs) inside the cell during charging is responsible for the oscillation of the potential drop across the cell observed in figure 2. To further rationalize how the formation of EDLs leads to the potential oscillation, we divide the space between the left wall and the middle plane of the cell into several layers: the first and the second layers (0 nm $< x <$ 0.93 nm and 0.93 nm $< x <$ 1.67 nm) correspond to the space occupied by the first counter-ion (anion) and co-ion (cation) layers adjacent to the left wall, respectively. The third layer (1.67 nm $< x <$ 2.31 nm) corresponds to the space occupied by the second layer of counter-ions near the wall. Since the alternating layering of counter-ions and co-ions is no longer strong beyond the second counter-ion peak, the space between $x = 2.31$ and 15 nm is taken as the fourth layer. It is worth noting that the locations of the counter-ion and co-ion layers adjacent to the wall will change during the charging process. However, such a change is relatively small during the time when potential oscillations are observed, and therefore we adopt a static partition of the ionic layers inside the cell. Figure 4(a) shows the evolution of the net charge in each of these layers and figures 4(b)–(d) show the detailed evolution of the cation density, anion density, space charge density and total ion density profiles during the first 6 ps of charging. We observe that the net charge grows noticeably only in the first layer at short times ($t <$ ~0.9 ps). The growth of the first layer is followed by the second, the third, and the fourth layers at successively later times.

Using the data on the growth of charge inside each layer shown in figures 4(a)–(c) and equation (5*c*), we compute how the sequential growth of all these layers contributes to the evolution of $\partial\phi_{ic}/\partial t$ with time. Figure 5(a) shows that, for $t <$ ~1 ps, if we include only the charge in the first space charge layer in ρ_e when evaluating equation (5*c*), the computed $\partial\phi_{ic}/\partial t$ is close to the result in which all space charge layers are included in ρ_e when evaluating equation (5*c*). This indicates that, for $t <$ ~1 ps, the growth of ϕ_{ic} is governed mostly by the growth of the first space charge layer (blue solid curve in figure 5(a)) and its competition with the growth of ϕ_{wc} due to the steady increase of wall charge density (solid black line in figure 5(a) leads to the first potential peak observed at $t \approx 0.9$ ps. Such an observation is expected because, by $t \sim 1$ ps, only the first space charge layer grows notably (i.e., has significant charge accumulation). Figure 5(a) also shows that at $t >$ ~1 ps, the growth of the first space charge layer contributes much more greatly to the variation of ϕ_{hc} than the growth of the wall charge. However, as can be seen from figure 5(b), while the growth of the first space charge layer tends to slow down the increase of ϕ_{hc}, its impact is strongly reduced by the growth of the second space charge layer. In fact, when the net charge in both layers is considered, $\partial\phi_{ic}/\partial t$ (thus $\partial\phi_{hc}/\partial t$) is small and even becomes smaller than $\partial\phi_{wc}/\partial t$ at $t \approx 1.46$ ps, which in turn leads to the first valley of the ϕ_{hc} at $t \approx 1.63$ ps. Such a result is consistent with the fact that, at $t > 0.9$ ps, the second space charge layer near the wall starts to grow rapidly (see figure 4(a)). Because the net charge in this layer is opposite to that in the first space charge layer, the growth of this layer counteracts the suppression effect on the growth of ϕ_{hc} due to the growth of the first space charge layer. Figure 5(b) shows that at $t > 1.63$ ps, the simultaneous growth of the first and the second charge layers tends to greatly enhance the growth of ϕ_{hc} (see blue line in figure 5(b)). However, as shown in figure 5(c), their effects are counteracted by the growth of the third space charge layer near the wall, which has a net charge opposite to that in the second space charge layer. While the large statistical noise in figure 5(c) prevents a conclusive determination of the origin of the second peak of ϕ_{hc} at $t \approx 2.84$ ps, it should be closely related to the significant growth of the third charge layer by this time. From figure 2, we also observe that there are more potential oscillations in smaller charging current cases, such as $I = 200$ kA cm^{-2}. This can be explained by the sequential formation of EDLs. During constant-current charging, the total charge on the wall at any given time is smaller for smaller current than that for higher current, then the formation of layers further away from the wall, such as the fourth and fifth layers, becomes more important in affecting the total potential drop in smaller charging current cases since the charges in those layers are more comparable to the total charge on the wall.

The above analysis shows that the sequential formation of the space charge layers with net charge of alternating

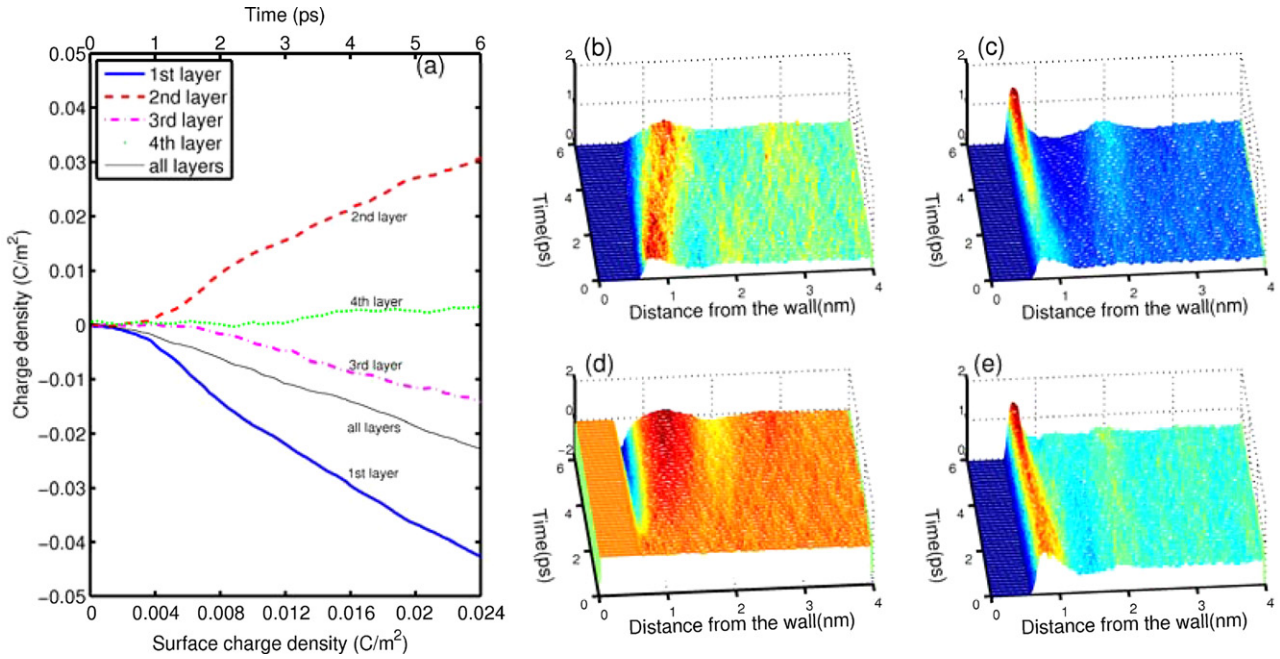

Figure 4. (a) Evolution of the net ionic space charge in the four layers defined in the text during the initial stage of charging. (b)–(e) Evolution of the cation number density, anion number density, space charge density and total number density, respectively, during the constant-current charging. $I = 400$ kA cm^{-2} in all cases.

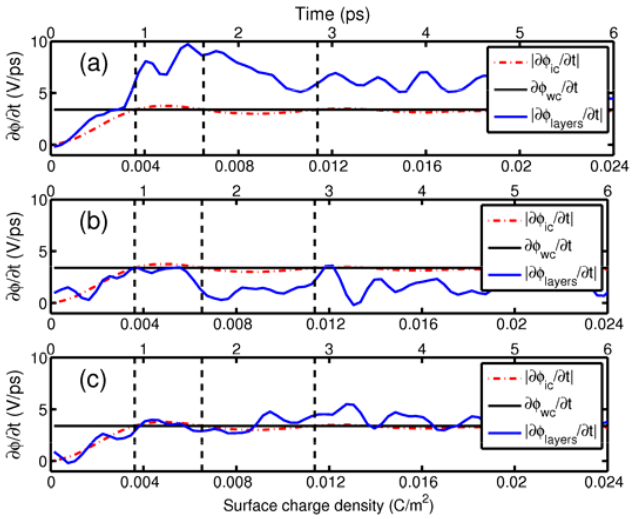

Figure 5. The evolution of $|\partial\phi_{ic}/\partial t|$ and how the growth of various space charge layers adjacent to wall contributes to it. Both $\partial\phi_{ic}/\partial t$ and $\partial\phi_{layers}/\partial t$ are negative, and so their absolute values are shown here to facilitate comparison with $\partial\phi_{wc}/\partial t$ (black solid line). The red dotted dashed curve denotes the contribution due to the space charge in all layers and the blue solid curve represents the potential due to the net charge in several layers ((a) the first layer only; (b) the first two layers; (c) the first three layers). The vertical black dashed line represents the time at which ϕ_{hc} reaches peak or valley. The charging current is $I = 400$ kA cm^{-2}.

signs causes the oscillation of the half-cell potential shown in figure 2. The origins of the sequential formation of the space charge layers near the wall can be understood as follows. Immediately after a constant current is imposed on the wall, the surface charge density on the walls starts to increase, creating an electric field across the cell to drive counter-ions (co-ions) toward (away from) each wall. Since the wall prevents penetration of counter-ions into them, counter-ions accumulate near the wall and thus the first space charge layer is the first to grow. With the lapse of time, the number of counter-ions inside the first layer increases more rapidly as the wall charge becomes larger (due to the constant-current charging). At $t \sim 0.8$ ps in the fastest charging case ($I = 400$ kA cm^{-2}), the rate at which the net charge inside the first layer increases becomes faster than that on the electrode walls. This phenomenon is analogous to the charge over-screening phenomenon in equilibrium EDLs and can be termed 'dynamic' over-screening. Because of this effect, co-ions are now attracted strongly toward the wall and the growth of the second space charge layer becomes prominent. Since the electrode walls are still being charged constantly, both the first and the second space charge layers continue to grow. In a similar manner, the third space charge layer starts to grow when the second space charge layer 'dynamically' over-screens the charge on the wall and inside the first space charge layer. Such a process is repeated in subsequent layers but becomes weaker as each additional layer is located farther away from the electrode wall.

4. Comparison between MD and continuum simulation results

In order to test the accuracy of the BSK model for non-equilibrium dynamics of RTILs, we also investigated the formation of EDLs under constant-current charging conditions using the continuum simulation approach described in section 2. Figure 6(a) shows that, at a current density of $I = 25$ kA cm^{-2}, the potential evolutions predicted by the MD and BSK models are in good agreement up to a relatively high wall

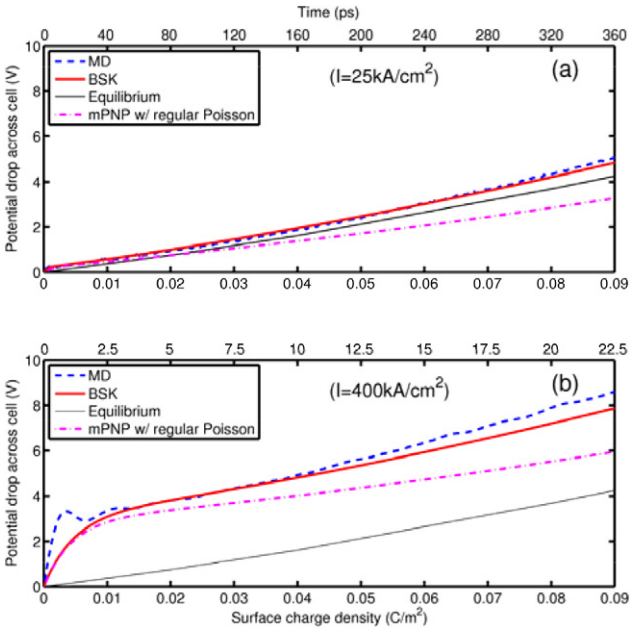

Figure 6. Evolution of potential drop across the entire cell predicted by MD, the BSK model and a modified PNP model with zero electrostatic correlation length (panel (a) $I = 25$ kA cm^{-2}, panel (b) $I = 400$ kA cm^{-2}). The equilibrium potential drop corresponding to various surface charge densities is computed in separate equilibrium MD simulations.

charge density of ∼0.07 C m^{-2}, suggesting that the BSK model can be used to quantitatively predict the formation of EDLs. This is quite encouraging as it opens the possibility of studying the charging dynamics in large systems using continuum simulations, which can be orders of magnitude faster than MD simulations. We also observe that the potential–surface charge relation obtained under such a current density already approaches that at equilibrium conditions, which, as explained in section 2, is caused by the fast diffusion of the model RTILs in our MD simulations.

Figure 6(b) compares the predictions of the potential drop across the entire cell by the MD and BSK models at the largest current density studied, i.e., $I = 400$ kA cm^{-2}. The BSK model cannot predict the fast rise of potential drop across the cell at the initial stage of charging as well as the potential oscillation until the surface charge density of electrode wall reaches ∼0.02 C m^{-2}. These difficulties most likely originate from the fact that the BSK model is parameterized to reproduce the structure and capacitance of the EDLs under equilibrium conditions and thus may not perform very well when the EDLs near the electrode wall are driven far from equilibrium, as is the present case under a very large charging current. For example, a dielectric constant of 5 was used in the parameterized BSK model. As clarified earlier, ionic polarization, i.e., the polarization due to relative displacements of oppositely charged ion pairs, contributes significantly to the overall dielectric screening both in bulk RTILs [40] and in EDLs [17]. When EDL formation is driven by a very large charging current, significant accumulation of net charge in space charge layers near the wall occurs at a time scale comparable to the time scale that an ion pair is polarized by external electric fields. Therefore, the effective dielectric constant experienced by the ions can be smaller than that at equilibrium conditions, akin to the scenario when bulk dielectric fluids (e.g., water) or electrolyte confined between two walls is subject to a strong external electric field imposed abruptly [41]. This helps explain the faster rise of cell potential during the initial stage of charging in MD simulations. Such effects may be incorporated into the BSK model by introducing a frequency-dependent dielectric constant, but this study is out of the scope of the present work. Figure 6(b) also shows that, at the later stage of charging (wall charge >0.045 C m^{-2}), the cell potential predicted by the BSK model increases at a slower rate compared to that observed in MD simulations. This is caused in part by the fact that a constant ion diffusion coefficient was used in the BSK model. When the wall charge density increases beyond ∼0.04 C m^{-2}, further growth of the ionic space charge layers is mainly due to the growth of the first ionic layer (MD results not shown). Since the counter-ion density inside the first ionic layer is already large at a wall charge density of 0.04 C m^{-2}, further insertion of counter-ions in this layer tends to reduce their diffusion coefficient in the direction normal to the electrode wall [42]. Such a decrease of the ion diffusion coefficient effectively increases the electrical resistance in the electrochemical cell, and consequently the potential drop across the cell from the MD simulations increases faster than that predicted by the BSK model, in which the ion diffusion coefficient is assumed to be uniform in the entire system and for the complete charging process.

Unlike previous modified PNP models, the BSK model effectively accounts for additional ion–ion correlations by introducing an electrostatic correlation length l_c into the Poisson equation (see equation (3)). To evaluate the importance of the ion–ion correlation effects, we also solved the BSK model by setting $l_c = 0$. In this case, the BSK model is reduced to the modified PNP model in [30], which only entertains steric effects. As shown in figure 6, such a modified PNP model performs considerably worse than the BSK model, and cannot even predict the charging kinetics at the lowest charging rate. This highlights the significance of parameterizing ion–ion correlation in the BSK model.

In addition to comparing the evolution of the electrical potential drop across the cell during charging, we performed a detailed comparison of the evolution of ion density profiles obtained by MD and the BSK model to further assess the accuracy of the BSK model in predicting the dynamics of double layer formation. To facilitate comparison, we divided the space between the right wall and middle plane into several layers following the partition method in [12]. The width of each layer is 1 nm, and the first layer is defined as the layer closest to the right wall. We next calculated the evolution of average cation/anion area densities in the first, second and third layers using MD and BSK models, and the results are shown in figure 7.

We observe that the unscaled ion densities in these layers (figures 7(a1-3)) in the MD simulation and BSK model differ even at $t = 0$, which makes the comparison of the evolution of unscaled ion densities at $t > 0$ difficult. The disagreement at $t = 0$ (when charge density on the wall is zero) is expected

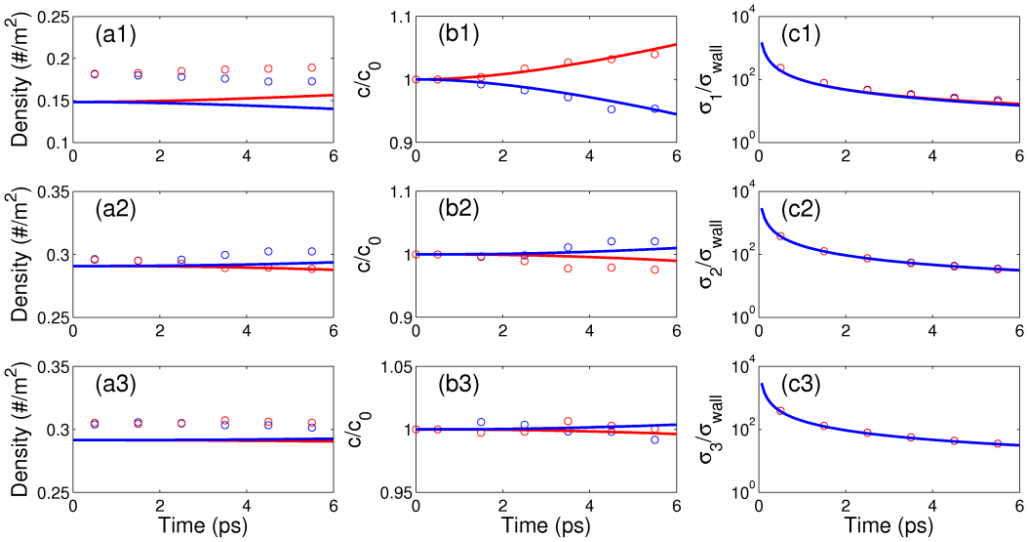

Figure 7. Temporal evolution of cation (red) and anion (blue) area densities in the first ((a1), (b1) and (c1)), second ((a2), (b2) and (c2)) and third ((a3), (b3) and (c3)) layers in the MD simulation at $I = 25$ kA cm^{-2} (dotted) and BSK model (solid line). (a1-3) are unscaled ion densities, (b1-3) are ion densities scaled by their initial value at $t = 0$ and (c1-3) are ion charge densities scaled by charge density on the wall, which increases with time. The method for partition of layers is the same as that in figure 3 of [12] and the width of each layer is 1 nm.

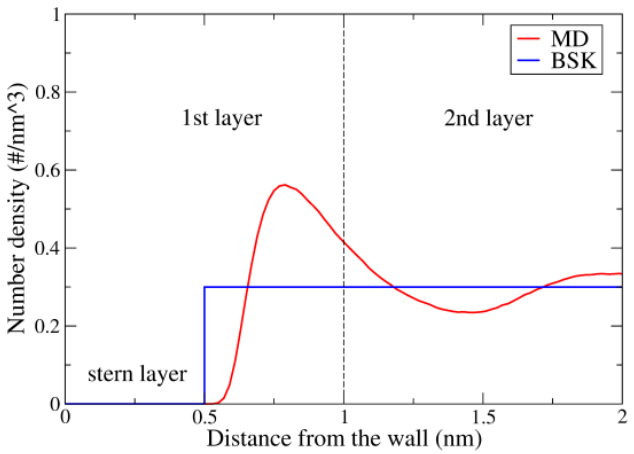

Figure 8. Ion densities near the wall when the wall is not charged in the MD and BSK models. Density profiles of cation and anion overlap with each other because the wall is electrically neutral.

because ion densities are non-uniform in MD system but uniform in the BSK model (see figure 8).

To circumvent the above issue, we scaled the ion densities in each layer by their values at $t = 0$. Figures 7(b1-3) show that in the first layer, the results from MD and BSK agree well with each other; in the second layer, ion densities predicted by MD model are slightly larger than by BSK and their agreement is fair; in the third layer, the noise in MD results prevents a conclusive comparison. Alternatively, we also scaled the cation and anion area charge densities (σ_{cation} and σ_{anion}) in each layer by the charge density on the wall, which increases with time during constant-current charging. Figures 7(c1-3) show that, in all layers, the orders of magnitude of $\sigma_{\text{cation}}/\sigma_{\text{wall}}$ and $\sigma_{\text{anion}}/\sigma_{\text{wall}}$ predicted by MD and BSK models agree well. Such an agreement is not trivial because, at short time, the magnitude of wall charge density σ_{wall} is very small. Note that the profiles of $\sigma_{\text{cation}}/\sigma_{\text{wall}}$ and $\sigma_{\text{anion}}/\sigma_{\text{wall}}$ nearly overlap with each other in all layers because the difference between cation and anion densities is quite small.

5. Conclusions

In summary, we have studied the dynamics of EDL formation at the interface of planar electrodes and RTILs under constant-current charging conditions. At relatively low charging rates, the evolution of the cell potential drop predicted by the MD simulations and the BSK model agree with each other quite well. At very high charging rates, MD simulations predict a very fast rise of the cell potential at very short times and an oscillation of the cell potential until the wall charge density reaches a moderate value ($\sim$0.02 C m^{-2} in our model). Such oscillation is caused by the sequential growth of the space charge layers with net charges of alternating signs near the electrode wall, and cannot be predicted by the present BSK model. In addition, the BSK model predicts a slower rise of cell potential during both the initial and later stages of charging compared to that obtained from MD simulations. Such a difference is most likely caused by the fact that the BSK model is parameterized under equilibrium conditions. This can in principle be resolved by introducing frequency-dependent dielectric constant, ion density-dependent diffusion coefficients and even local concentration/field-dependent l_c into the BSK model [43, 44]. Together, these results suggest that, unless EDL formation occurs under far-from-equilibrium conditions, its macroscopic behavior can be predicted quite well by the BSK model. The evolution of ion density profiles, another aspect of the EDL formation dynamics, is also compared to further assess the accuracy of the BSK model in predicting the dynamics of double layer formation, showing good agreement between the MD and BSK models.

The present study suggests that one can gain insights into the formation of separate EDL layers, an atomistic process difficult to quantify directly, by analyzing the oscillation of the electrical potential as a function of time during a constant-current charging process. Such a procedure can also potentially provide critical information about the ion transport behavior within the EDL and in the direction normal to the electrode wall. However, the experimental studies of galvanostatic charge/discharge of supercapacitors utilizing RTILs as electrolytes do not display such potential oscillations, probably because of the limited temporal resolution on a time scale of seconds. In the model RTIL we employed, the potential oscillation is observed at very large charging current ($>O(100$ kA cm^{-2})) and very short time scale ($<O(5$ ps)). As pointed out above, this is mainly caused by the large diffusion coefficient of the model RTILs, which enables very fast formation/relaxation of the EDL structure and potential. Consequently, a far-from-equilibrium EDL formation can only be probed using large charging currents and observed at short time scales. For practical RTILs, whose diffusion coefficient is usually three to four orders of magnitude smaller than the model RTIL considered here, the formation/relaxation of the EDL is much slower and thus we can expect the potential oscillation to be observed at charging currents that are more accessible experimentally and at much longer time scales up to 1 ns. Nevertheless, the temporal resolution of present galvanostatic charge/discharge experiments must be enhanced to the nanosecond scale in order to observe the potential oscillations predicted in this work.

Acknowledgments

The authors thank the Clemson-CCIT office for providing computer time. The authors thank Professor Martin Bazant (MIT) and Professor Brian Storey (Olin College) for critical reading of our draft manuscript and helpful discussions. The Clemson authors acknowledge support from NSF under Grant No. CBET-1264578. RQ was partially supported by an appointment to the HERE program for faculty at the Oak Ridge National Laboratory (ORNL) administered by ORISE. The authors at ORNL acknowledge the support from the Center for Nanophase Materials Sciences, which is sponsored at ORNL by the Scientific User Facilities Division, Office of Basic Energy Sciences, US Department of Energy.

References

[1] Ohno H (ed) 2005 *Electrochemical Aspects of Ionic Liquids* (New York: Wiley)
[2] Freemantle M 2009 *An Introduction to Ionic Liquids* (Cambridge: The Royal Society of Chemistry)
[3] Baldelli S 2013 *J. Phys. Chem. Lett.* **4** 244
[4] Penalber C Y, Baker G A and Baldelli S 2013 *J. Phys. Chem.* B **117** 5939
[5] Tamura K, Miyaguchi S, Sakaue K, Nishihata Y and Mizuki J 2011 *Electrochem. Commun.* **13** 411
[6] Yoshimoto S, Taguchi R, Tsuji R, Ueda H and Nishiyama K 2012 *Electrochem. Commun.* **20** 26
[7] Perkin S 2012 *Phys. Chem. Chem. Phys.* **14** 5052
[8] Perkin S, Crowhurst L, Neidermeyer H, Welton T, Smith A M and Gosvami N N 2011 *Chem. Commun.* **47** 6572
[9] Zhang X, Zhong Y X, Yan J W, Su Y Z, Zhang M and Mao B W 2012 *Chem. Commun.* **48** 582
[10] Kornyshev A A 2007 *J. Phys. Chem.* B **111** 5545
[11] Oldham K B 2008 *J. Electroanal. Chem.* **613** 131
[12] Bazant M Z, Storey B D and Kornyshev A A 2011 *Phys. Rev. Lett.* **106** 046102
[13] Fedorov M V and Kornyshev A A 2008 *Electrochim. Acta* **53** 6835
[14] Jiang X K and Qiao R 2012 *J. Phys. Chem.* C **116** 1133
[15] Wang S, Cao Z, Li S and Yan T Y 2009 *Sci. China, Ser.* B **52** 1434
[16] Kislenko S A, Samoylov I S and Amirov R H 2009 *Phys. Chem. Chem. Phys.* **11** 5584
[17] Feng G, Huang J S, Sumpter B G, Meunier V and Qiao R 2011 *Phys. Chem. Chem. Phys.* **13** 14723
[18] Feng G, Jiang D E and Cummings P T 2012 *J. Chem. Theory Comput.* **8** 1058
[19] Shim Y S and Kim H J 2013 *J. Phys. Chem.* B **117** 11743
[20] Hooper J B, Starovoytov O N, Borodin O, Bedrov D and Smith G D 2012 *J. Chem. Phys.* **136** 194506
[21] Jiang D E and Wu J Z 2013 *J. Phys. Chem. Lett.* **4** 1260
[22] Singh R, Rajput N N, He X X, Monk J and Hung F R 2013 *Phys. Chem. Chem. Phys.* **15** 16090
[23] Singh R, Monk J and Hung F R 2011 *J. Phys. Chem.* C **115** 16544
[24] Rajput N N, Monk J and Hung F R 2012 *J. Phys. Chem.* C **116** 14504
[25] Singh R, Monk J and Hung F R 2010 *J. Phys. Chem.* C **114** 15478
[26] Rajput N N, Monk J, Singh R and Hung F R 2012 *J. Phys. Chem.* C **116** 5169
[27] Lanning O J and Madden P A 2004 *J. Phys. Chem.* B **108** 11069
[28] Pinilla C, Del Popolo M G, Kohanoff J and Lynden-Bell R M 2007 *J. Phys. Chem.* B **111** 4877
[29] Vatamanu J, Borodin O and Smith G D 2011 *J. Phys. Chem.* B **115** 3073
[30] Kilic M S, Bazant M Z and Ajdari A 2007 *Phys. Rev.* E **75** 021503
[31] Storey B D and Bazant M Z 2012 *Phys. Rev.* E **86** 056303
[32] Zhao H 2011 *Phys. Rev.* E **84** 051504
[33] Pronk S *et al* 2013 *Bioinformatics* **29** 845
[34] Largeot C, Portet C, Chmiola H, Taberna P-L, Gogotsi Y and Simon P 2008 *J. Am. Chem. Soc.* **130** 2730
[35] Pushparaj V, Shaijumon M M, Kumar A, Murugesan S, Ci L J, Vajtai R, Linhardt R J, Nalamasu O and Ajayan P M 2007 *Proc. Natl Acad. Sci. USA* **104** 13574
[36] Feng G, Zhang J S and Qiao R 2009 *J. Phys. Chem.* C **113** 4549
[37] *Comsol Multiphysics 4.2 User Guide* Burlington, United States, 2011
[38] *Comsol Multiphysics 4.2 Reference Guide* Burlington, United States, 2011
[39] Frackowiak E 2007 *Phys. Chem. Chem. Phys.* **9** 1774
[40] Izgorodina E I, Forsyth M and MacFarlane D R 2009 *Phys. Chem. Chem. Phys.* **11** 2452
[41] Cagle C, Feng G, Qiao R, Huang J S, Sumpter B G and Meunier V 2010 *Microfluid. Nanofluid.* **8** 703
[42] Sendner C, Horinek D, Bocquet L and Netz R R 2009 *Langmuir* **25** 10768
[43] Bazant M Z, Kilic M S, Storey B D and Ajdari A 2009 *Adv. Colloid Interface Sci.* **152** 48–88
[44] Bazant M Z 2013 *Acc. Chem. Res.* **46** 1144–60